# Application of the relativistic mean-field mass model to the *r*-process and the influence of mass uncertainties

B. Sun (孙保华),[1,2,*] F. Montes,[2,3] L. S. Geng (耿立升),[1,4] H. Geissel,[2] Yu. A. Litvinov,[2] and J. Meng (孟杰)[1,5,6,7,†]

[1]*School of Physics and State Key Laboratory of Nuclear Physics and Technology, Peking University, 100871 Beijing, China*

[2]*Gesellschaft für Schwerionenforschung GSI, D-64291 Darmstadt, Germany*

[3]*National Superconducting Cyclotron Laboratory, Michigan State University, East Lansing, Michigan 48824, USA*

[4]*Departamento de Física Teórica and IFIC, Centro Mixto Universidad de Valencia-CSIC, Institutos de Investigación de Paterna, Aptdo. 22085, 46071 Valencia, Spain*

[5]*Department of Physics, University of Stellenbosch, Stellenbosch, South Africa*

[6]*Institute of Theoretical Physics, Chinese Academy of Sciences, Beijing, China*

[7]*Center of Theoretical Nuclear Physics, National Laboratory of Heavy Ion Accelerator, 730000 Lanzhou, China*

(Received 20 February 2008; revised manuscript received 16 June 2008; published 21 August 2008)

A new mass table calculated by the relativistic mean-field approach with the state-dependent BCS method for the pairing correlation is applied for the first time to study *r*-process nucleosynthesis. The solar *r*-process abundance is well reproduced within a waiting-point approximation approach. Using an exponential fitting procedure to find the required astrophysical conditions, the influence of mass uncertainty is investigated. The *r*-process calculations using the FRDM, ETFSI-Q, and HFB-13 mass tables have been used for that purpose. It is found that the nuclear physical uncertainty can significantly influence the deduced astrophysical conditions for the *r*-process site. In addition, the influence of the shell closure and shape transition have been examined in detail in the *r*-process simulations.

DOI: 10.1103/PhysRevC.78.025806 PACS number(s): 21.10.Dr, 21.60.Jz, 23.40.Hc, 26.30.Hj

## I. INTRODUCTION

It is of the utmost interest to explore the "terra incognita" of exotic nuclei, as evidenced by the fact that several radioactive ion beam (RIB) facilities are being upgraded, under construction, or planned to be constructed worldwide. Such investigations of the properties of these exotic nuclei, which may behave very differently from the nuclei around the $\beta$-stability line, result in new discoveries such as the halo phenomenon [1,2]—nucleons spread like a thin mist around the nucleus, which can significantly increase the nuclear reaction ratio. Stellar nucleosynthesis processes such as the *r*-process [3,4], which is responsible for roughly half of the enrichment of elements heavier than iron in the universe, also require a thorough understanding of the properties of exotic nuclei. Key properties such as masses, for example, determine the path that the nucleosynthesis process follows in the nuclei chart. Nevertheless, despite many experimental efforts, present knowledge of exotic nuclei still does not include much of what is required for a complete understanding of *r*-process nucleosynthesis. After the first systematic introduction to the *r*-process [5] half a century ago, *r*-process calculations for a long time could only rely on the phenomenological nuclear droplet mass formula [6] because of the lag in both experimental and theoretical development. Fortunately, in the past 15 years the theoretical study of nuclear properties has made tremendous progress and *r*-process calculations [7–9] have been carried out based on the refined droplet model FRDM [10], Hartree-Fock approaches such as ETFSI-Q [11], and the very recent microscopically rooted Hartree-Fock Bogliubov (HFB) approach [12–14].

Despite progress in theoretical nuclear structure physics, mass model predictions (which by design concentrate on different nuclear structure aspects) still show a large deviation when going to very neutron rich nuclides, even though they have achieved similar quality to describe known nuclides. This is especially troublesome since the astrophysical scenario in which an *r*-process may occur is a matter of debate and all astrophysical simulations dedicated to the nature of the stellar environment depend on the input from nuclear physics. Mass model predictions, even in models that give similar global rms error still show local deviations differently.

In principle, microscopically rooted mass models should have a more reliable extrapolation to the unknown regions; therefore these studies have received more and more interest as evidenced by the increasing number of nonrelativistic HFB investigations [12–15]. Based on a mass-driven fitted method, the latest HFB models have achieved a quality (with rms $\sim 0.7$ MeV) similar to the phenomenological FRDM mass model for known masses. More recently, another microscopically rooted approach, relativistic mean-field (RMF) theory [16], has received broad attention owing to its successful description of several nuclear phenomena during the past few years (for recent reviews, refer to Refs. [17,18]). In the framework of RMF theory, the nucleons interact via the exchanges of mesons and photons. The corresponding large scalar and vector fields, of the order of a few hundred MeV, provide simple and efficient descriptions of several important phenomena such as the large spin-orbit splitting, the density dependence of the optical potential, and the observation of approximate pseudo-spin symmetry. Moreover, RMF theory can reproduce well the isotopic shifts in the Pb region [19]

*B.Sun@gsi.de
†mengj@pku.edu.cn

 

and explain naturally the origin of the pseudo-spin symmetry [20,21] as a relativistic symmetry [22–25] and spin symmetry in the anti-nucleon spectrum [26].

The first RMF mass table was reported in Ref. [27] for 2174 even-even nuclei with $8 \leqslant Z \leqslant 120$ but without including pairing correlations. Later on, the calculation was improved by adopting a constant-gap BCS method and 1200 even-even nuclei with $10 \leqslant Z \leqslant 98$ were calculated [28], most of which are close to the $\beta$-stability line. More recently, by using the state-dependent BCS method with a $\delta$ force [29,30], the first systematic study of the ground-state properties of over 7000 nuclei ranging from the proton dripline to the neutron dripline was performed [31]. Comparison of this calculation with experimental data and to the predictions of other mass models will be presented in more detail in Sec. II.

Considering the recent development of the microscopic mass models in both the HFB and RMF approach, we thought it would be very interesting to examine their applicability to an $r$-process calculation. The main goals of this paper are to explore to what extent the solar $r$-process abundance can be reproduced by using the new RMF mass table [31] and, by comparing with other theoretical mass models, to determine the influence of nuclear mass uncertainty in $r$-process calculations. The paper is organized as follows. In Sec. II the global agreement of the new RMF mass table with the experimental data is discussed and the RMF prediction in the very neutron rich range is compared with the FRDM [10], the ETFSI-Q [11], and the latest HFB-13 [15] mass tables. In Sec. III, a short introduction to a site-independent $r$-process approach is given. In Sec. IV, the new mass table is applied to reproduce the solar $r$-process abundances. In addition, the result is compared to the $r$-process abundances obtained with the predictions of the FRDM, ETFSI-Q, and HFB-13 mass models. Finally, a summary and conclusions are given in Sec. V.

## II. GLOBAL BEHAVIOR OF THE NEW RMF MASS TABLE

With about 10 parameters fitted to the ground-state properties of around 10 spherical nuclei, the RMF approach with the TMA parameter set is found to give a satisfactory description for all nuclei on the nuclear chart. The model deviation of one-neutron separation energy $S_n$ with respect to the known experimental data can be characterized by the rms deviation

$$\sigma_{\mathrm{rms}} = \sqrt{\frac{1}{n}\sum_{i=1}^{n}\left(S_n^{\mathrm{th}} - S_n^{\mathrm{exp}}\right)_i^2}. \qquad (1)$$

Although a relatively large rms deviation for the absolute mass value is found for the RMF calculation in comparison with the FRDM and HFB-13 models, the finite differences in binding energies, such as the practical one-neutron separation energies $S_n$ used, are well predicted owing to the cancellation of systematic error [31,32]. The rms deviation of $S_n$ for the FRDM, ETFSI-Q, HFB-13, and RMF models with respect to experimentally determined values [33] are 399, 528, 546, and 654 keV, respectively. Here the comparisons include nuclei with $Z, N \geqslant 8$. Comparing the predictions of the RMF model

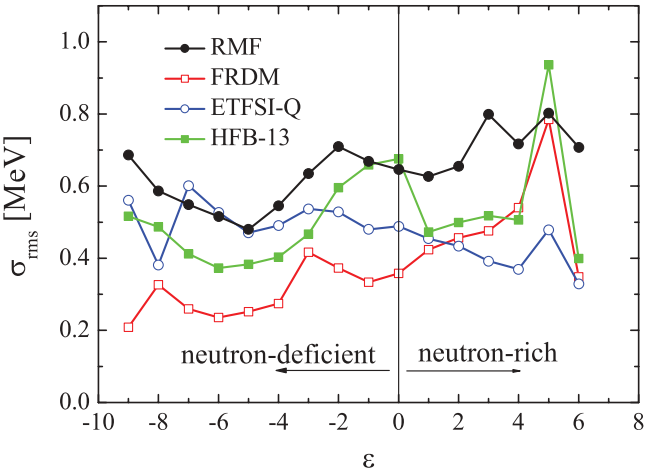


FIG. 1. (Color online) The rms deviation $\sigma_{\mathrm{rms}}$ of one-neutron separation energy $S_n$ with respect to experimental data [33] as a function of the distance from the $\beta$-stability line $\varepsilon = Z_0 - Z$ for different mass models, where $Z_0$ stands for the proton number of the most stable isotope in the isobaric chain with mass number $A$.

to the known values [33] results in discrepancies between $-1.4$ to 1 MeV, and the difference between either the FRDM or the HFB-13 and the experimental data is in the range of $-1.3$ to 0.5 MeV. This shows that the microscopic model such as the RMF approach can achieve almost the same level of accuracy for known one-neutron separation energy $S_n$ as the phenomenological FRDM. For each isobaric chain with mass $A$, the distance between the nuclide $(Z, A)$ and the nuclide $(Z_0, A)$ in the $\beta$-stability line [34] is defined by $\varepsilon = Z_0 - Z$ with

$$Z_0 = \frac{A}{1.98 + 0.0155A^{2/3}}; \qquad (2)$$

that is, $\varepsilon = 0$ stands for the most stable nuclei and $\varepsilon > 0$ for the neutron-rich nuclei. The rms deviation $\sigma_{\mathrm{rms}}$ of $S_n$ as a function of $\varepsilon = Z_0 - Z$ for different mass models is shown in Fig. 1. It is remarkable that almost the same order of prediction power of $S_n$ from the neutron-deficient side to the neutron-rich side is achieved for all the models, even though models such as FRDM and HFB-13 have about 10 more free parameters than the RMF model and were optimized for all the known masses. Although the macroscopic-microscopic mass model FRDM shows the best agreement with experimental values in the neutron-deficient mass region, it gets progressively worse when moving away from the stability line toward the neutron-rich side.

All theoretical models addressing nuclei far from the $\beta$-stability line involve a dramatic extrapolation to unknown nuclei. Thus it is interesting to examine the difference of $S_n$ predicted in the different models when going toward the neutron-rich side. In Fig. 2, the differences between $S_n$ in the RMF model and those in the HFB-13 mass models are shown as an example. In general, most of the discrepancies between the two microscopic models range from $-1$ to 1 MeV across the entire nuclear chart. Furthermore, the $S_n$ value is consistent with that in the HFB-13 model in the range of $-0.5$ to 0.5 MeV when going to the unknown region of the nuclear

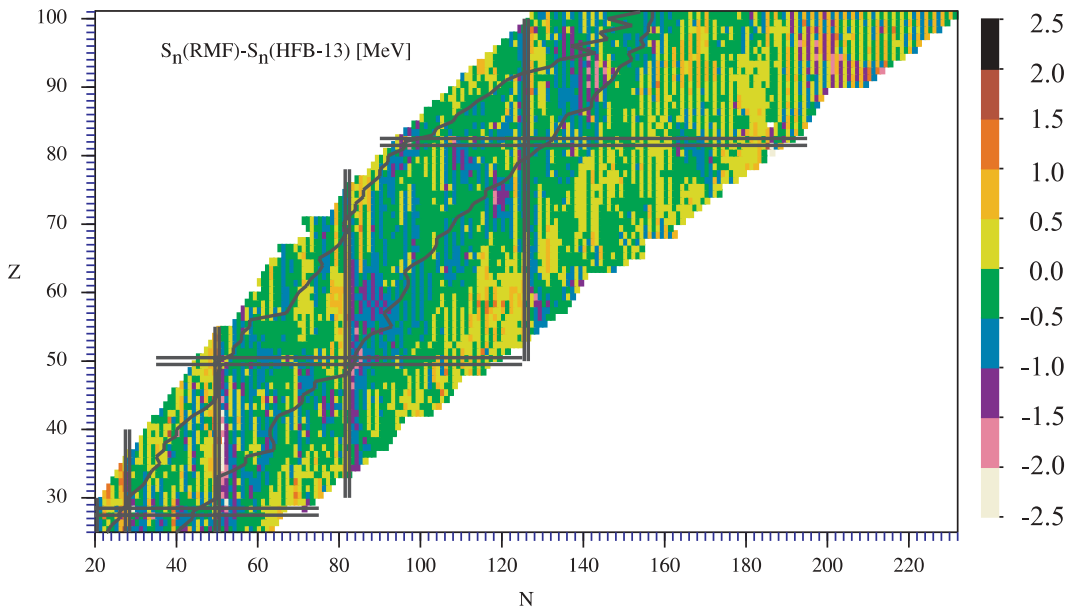


FIG. 2. (Color online) The differences between one-neutron separation energies $S_n$ predicted in the RMF model and those in the HFB-13 model. The magic proton and neutron numbers are indicated by pairs of parallel lines, and also the present borders of the data with known masses are shown by solid lines.

chart. These differences indicate that the extrapolation can be quite different depending on the underlying physics of the model. A similar conclusion can be drawn also for the comparison of the RMF and FRDM models. Around the $N = 82$ shell, the RMF model predicts a systematically lower $S_n$. These different $S_n$ predictions toward the neutron dripline affect $r$-process calculations and thus the corresponding determined astrophysical conditions.

The evolution of the nuclear structure around the shell closures $N = 82$ and 126 is critical in understanding the $r$-process abundance distribution around the $A = 130$ and $A = 195$ abundance peaks. At the shell closures, the one-neutron separation energy drops, and thus the corresponding nucleus in the $r$-process path cannot absorb another neutron without photodisintegration. Therefore it has to "wait" for the $\beta$ decay to proceed, and the path moves closer to the valley of stability where the half-lives are longer. These isotopes with long half-lives serve as bottlenecks of the process where abundances accumulate and the abundance peaks are formed. In Fig. 3, the predicated average one-neutron separation energy $S_{2n}/2$ around $N = 82$ in the RMF model is displayed as a function of mass number for isotopes from Kr to Ba together with the experimental values and the predictions of the FRDM, ETFSI-Q, and HFB-13 models. The dominating isotopes in the $r$-process path (defined as waiting points and discussed in Sec. IV) are also indicated for the corresponding mass model. Similarly, Fig. 4 presents the $S_{2n}/2$ distribution around the $N = 126$ shell for isotopes from Ce to Pt. In general, the RMF model reproduces well the experimental data and predicts a much more subtle variance relative to other mass models. The neutron shell gaps, defined as $\Delta_n(Z, A) = S_{2n}(Z, A) - S_{2n}(Z, A + 2)$, can be more clearly seen from Fig. 5, which shows the shell gaps for $N = 82$ and 126 in the RMF approach in comparison with the data available and those in the FRDM, ETFSI-Q, and HFB-13 models. The nuclei in the shadowed area are in the $r$-process path. At the $N = 82$ shell, all the mass models except the FRDM model show a strong quenching effect (i.e., the shell gap drops) toward the neutron-rich side. The RMF shell gap is overestimated compared with the data available and it is around 2 MeV larger than that for other models for $45 \leqslant Z \leqslant 60$. Nonetheless, the RMF model succeeds in predicting the enhanced double-magic effect at $Z = 50$ together with the HFB-13 model. For $N = 126$, there is no sign of shell quenching observed in the $r$-process region for any of the models. A unique feature of the RMF model is that it fully coincides with the available data and it is also the only model to reproduce the enhanced double-magic effect at $Z = 82$. In comparison, the other models fail to reproduce the trend of the known $N = 126$ shell. Toward the neutron dripline, the RMF prediction tends to enhance the shell until the maximum is reached around $Z = 60$ whereas the other models have a roughly constant shell gap.

## III. SITE-INDEPENDENT $r$-PROCESS APPROACH

Since the $r$-process is responsible for the synthesis of half the heavier nuclei beyond the iron group [3,4], the basis of the nucleosynthesis mechanism has been extensively studied. Nevertheless, the location where it occurs has not been unambiguously identified. Current location candidates include the neutrino-driven wind off a proton-neutron star in core collapse supernovae [35–38], neutron star mergers [39–41], jets in core collapse supernovae [42], shocked surface layers of O-Ne cores [43], and $\gamma$-ray bursts [44]. Because the specific

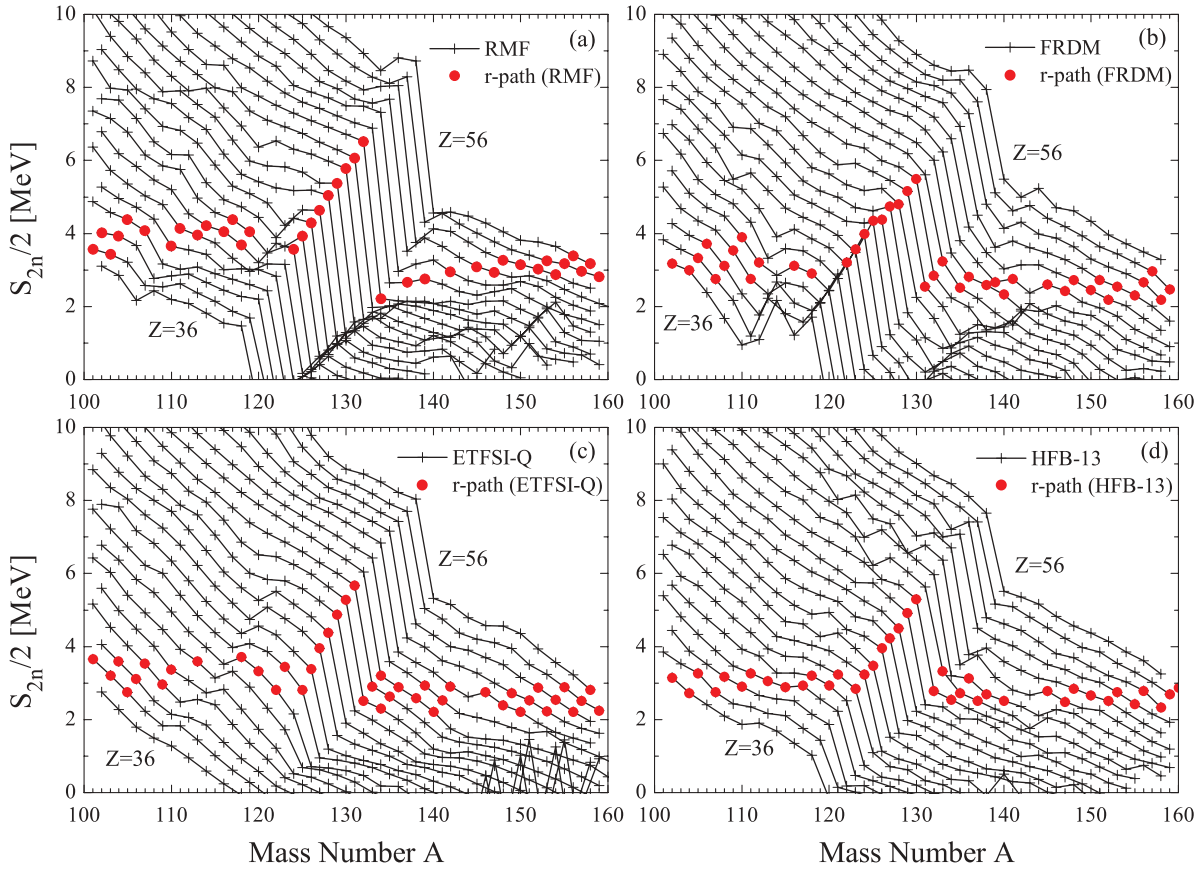


FIG. 3. (Color online) The average one-neutron separation energies around the $N = 82$ shell in the RMF model, in comparison with those in the FRDM, ETFSI-Q, and HFB-13 models as a function of mass number $A$. For simplicity only nuclei with even $N$ are plotted. The corresponding $r$-process paths calculated by using different mass inputs are also indicated by dots, and labeled here are those isotopes with more than 10% population of each isotopic chain.

astrophysical conditions among the different scenarios may change, solar $r$-process abundances [45] have been used in the past to constrain the astrophysical conditions by using a site-independent approach [7,46]. In this approach seed nuclei (usually the iron group) are irradiated by neutron sources of high and continuous neutron densities $n_n$ ranging from $10^{20}$ to $10^{28}$ cm$^{-3}$ over a time scale $\tau$ in a high-temperature environment ($T \sim 1$ GK). This superposition of $r$-process components $(n_n, \tau)$ is needed to reproduce the overall shapes and positions of the solar $r$-process abundances [7,8,47] and it is equivalent to the exponential neutron exposures in the $s$-process [48]. The configuration of many $r$-process components seems to be also a reasonable approximation to the real $r$-process event. For instance, one can think of it as the "onion" structure of neutron sources with different densities, where the seed nuclei capture neutrons while moving through different zones with different thicknesses. In this paper we explore for the first time the application of the new RMF mass model to an $r$-process calculation and at the same time investigate the effect of nuclear physics uncertainty in the $r$-process.

Owing to the high neutron densities, neutron captures are much faster than the competing $\beta$ decays and an $(n, \gamma) \Leftrightarrow (\gamma, n)$ equilibrium is nicely established for every element. The abundance ratio of two isotopes on a time scale $\tau$ can be expressed simply as

$$\frac{Y(Z, A+1)}{Y(Z, A)} = n_n \left(\frac{h^2}{2\pi m_\mu \kappa T}\right)^{3/2} \frac{G(Z, A+1)}{2G(Z, A)} \left(\frac{A+1}{A}\right)^{3/2} \times \exp\left[\frac{S_n(Z, A+1)}{\kappa T}\right], \quad (3)$$

where $Y(Z, A)$ denotes the abundance of the nuclide $(Z, A)$, $S_n$ is the one-neutron separation energy, $G(Z, A)$ is the partition function of nuclide $(Z, A)$, and $h, \kappa$, and $m_\mu$ are the Planck constant, Boltzmann constant, and atomic mass unit, respectively. Neglecting the difference in the ratios of the partition functions and the atomic mass, one can easily see that the isotopic abundance distribution $P(Z, A)$ and the abundance maxima in each isotopic chain are determined by $n_n, T$, and $S_n$. By approximating $Y(Z, A+1)/Y(Z, A) \simeq 1$ at the highest isotopic abundance for each element, and with all other quantities being constant, the average neutron-separation

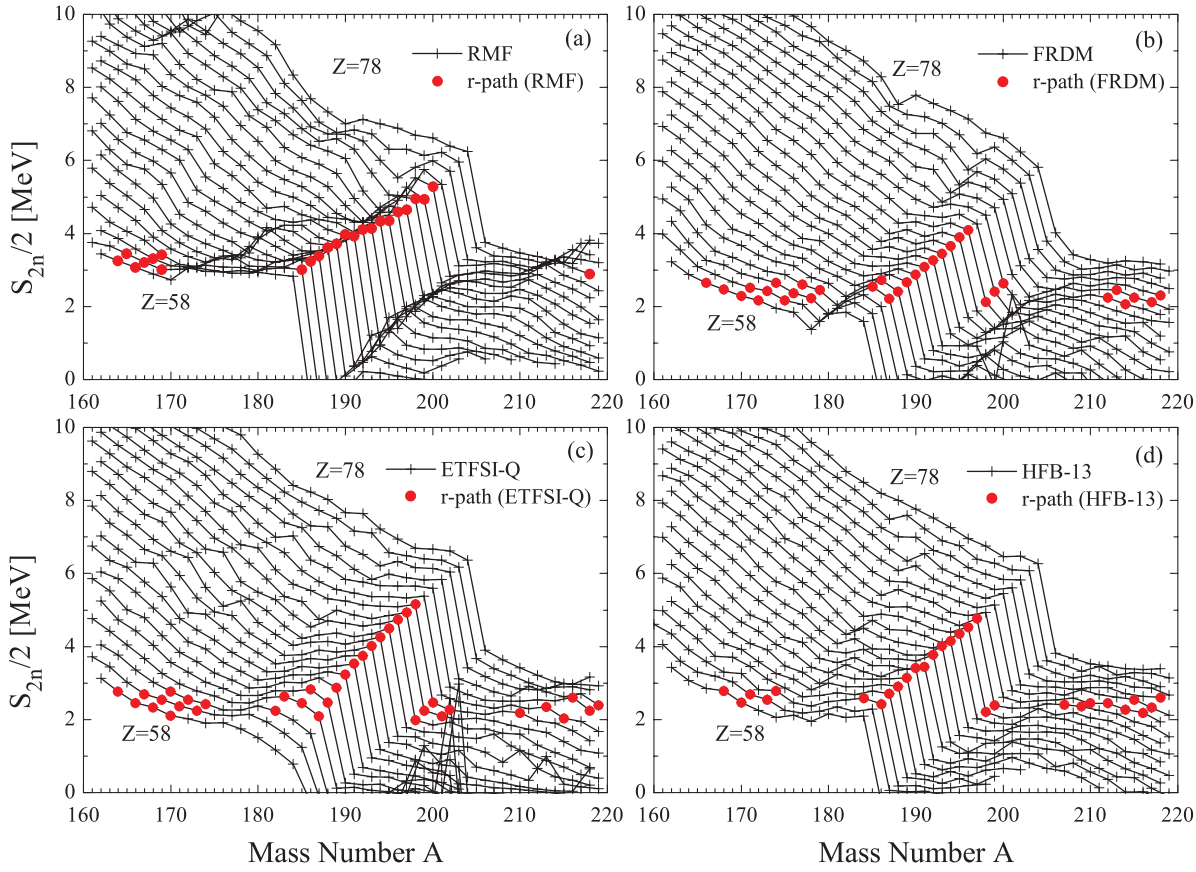


FIG. 4. (Color online) Same to Fig. 3 but around the $N = 126$ shell.

energy $\bar{S}_n$, calculated by

$$\bar{S}_n \approx \kappa T \log\left[\frac{2}{n_n}\left(\frac{2\pi m_\mu \kappa T}{h^2}\right)^{3/2}\right] = T_9\left\{2.79 + 0.198\left[\log\left(\frac{10^{20}}{n_n}\right) + \frac{3}{2}\log T_9\right]\right\}, \quad (4)$$

where $T_9$ denotes the temperature in $10^9$ K, is the same for all the nuclides with the highest abundance in each isotopic chain. Higher temperature or lower neutron density will drive the $r$-process path toward the valley of stability. Owing to the pairing correlation the most abundant isotope always has an even neutron number $N$.

If fission is neglected, the abundance flow from one isotopic chain to the next is governed by $\beta$ decays and can be expressed by a set of differential equations:

$$\frac{dY(Z,A)}{dt} = Y(Z-1)\sum_A P(Z-1,A)\lambda_\beta^{Z-1,A} - Y(Z)\sum_A P(Z,A)\lambda_\beta^{Z,A}, \quad (5)$$

where $\lambda_\beta^{Z,A}$ is the total decay rate of the nuclide $(Z, A)$ via the $\beta$ decay and the delayed neutron emission, and $Y(Z) = \sum_A Y(Z,A) = \sum_A P(Z,A)Y(Z)$ is the total abundance in each isotopic chain. By using Eqs. (3) and (5), the abundance for each isotope can be calculated. After the neutrons freeze out all the isotopes will proceed to the corresponding stable isotopes via $\beta$ decays.

## IV. CALCULATIONS

In the present calculation, unknown one-neutron separation energies $S_n$ were calculated from the RMF approach [31] and $\beta$-decay properties were taken from Ref. [49]. Experimental data [33,50] were used when available. Similar to the method used in Refs. [8,46,47], we applied 16 components with neutron densities in the range of $10^{20}$ to $3 \times 10^{27}$ cm$^{-3}$ in our calculation. We chose a temperature $T = 1.5$ GK. We assumed that for this temperature the irradiation time $\tau$ and the corresponding weight $w$ follow an exponential dependence on neutron density $n_n$, that is,

$$w(n_n) = n_n^a, \quad \tau(n_n) = b \times n_n^c, \quad (6)$$

where $a$, $b$, and $c$ are parameters to be fixed. These parameters can be obtained from a least-square fit to the solar $r$-process abundances. We further assume that the longest neutron irradiation time has to be longer than 0.5 s but shorter than 20 s. The exponential relations in Eq. (6) have been observed when fitting the three $r$-process peaks [51] and used for stellar and chronometer studies [8,47,52].

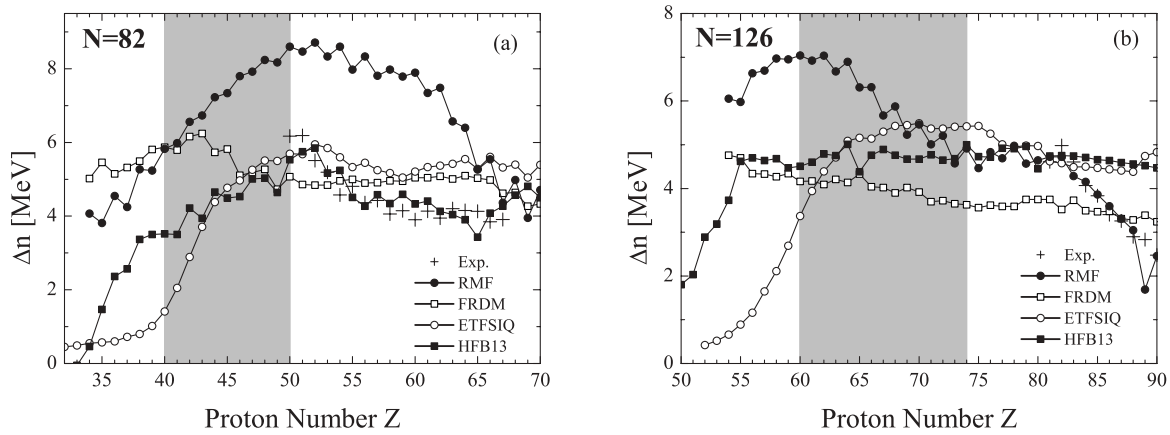


FIG. 5. The neutron shell gaps $\Delta_n(Z, A) = S_{2n}(Z, A) - S_{2n}(Z, A + 2)$ for $N = 82$ and 126 in the RMF approach compared with those in the FRDM, ETFSI-Q, and HFB-13 models together with the data available. The nuclei in the shadowed areas are involved in the $r$-process paths based on our calculations.

It was found that $r$-process components with $\tau(n_n) = 0.454 n_n^{0.040}$ s and $w(n_n) = 2.1 n_n^{0.02}$ best reproduce the solar $r$-process abundance. Figure 6 shows the contribution of the four group-weighted $r$-process components after $\beta$ decays to the resulting best fit. The black solid curve with isotopic abundances normalized to $A = 130$ corresponds to the fit using all 16 components. The green, red, blue, and gray dashed curves are the sum of the abundances calculated with $\log(n_n)$ ranging from 20 to 22.5, 13 to 24.5, 25 to 26.5, and 27 to 27.5, respectively. The first six components with $\log(n_n)$ between 20 and 22.5 seem to account for the $A = 80$ abundance peak. The four components with $\log(n_n)$ between 23 and 24.5 are responsible for the overall structure of the $r$-abundance curve beyond $A = 120$ and the remaining components only improve the description of the theoretical calculation for $A > 150$. In general, the fit is found to reproduce well the solar $r$-process abundances and also the position of the abundance peaks.

The $r$-process runs relatively close to the $\beta$-stability line around the shell closure; thus the experimentally known mass values around $N = 82$ shell significantly influence the abundance distribution after the second abundance peak. Taking our best simulation using the RMF masses as an example, we find that the ratio between the abundance at $A = 130$ and the abundance at $A = 195$ is 2.8 when taking the experimental data into account, and it increases to 24.6 if the experimental data are not used. The same ratio decreases from 4.0 to 1.3 for the best simulation using the FRDM masses (to be discussed in the following). To minimize the contribution from the theoretical uncertainty of known masses, experimental information was included in the calculations.

To investigate the impact of theoretical uncertainty of unknown masses in an $r$-process calculation, we also performed the same procedure using instead the FRDM, ETFSI-Q, and HFB-13 mass predictions while keeping the same $\beta$-decay properties. The astrophysical conditions determined by using various mass inputs are shown in Fig. 7. The obtained superpositions of 16 $r$-process components for all the mass tables are collected in Table I. Similar to the astrophysical conditions obtained from ETFSI-Q simulations, the astrophysical condition found using the RMF mass input requires a relatively constant weighting factor for different neutron densities. However, the FRDM and HFB-13 cases favor a large weighting factor for low neutron density. For the neutron irradiation time, the best RMF fit requires component durations of as long as 6 s whereas the FRDM and HFB-13 simulations require only up to 1.5 s. The ETFSI-Q component

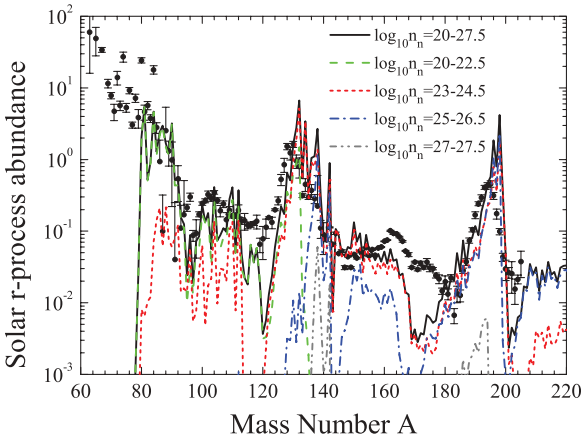


FIG. 6. (Color online) The effect of various weighted $r$-process components on the resulting fit after $\beta$ decays in the best superposition using the RMF masses. The calculated total isotopic abundances (on a logarithmic scale) are normalized to $A = 130$.

TABLE I. Our best fits to the solar $r$-process abundances for different sets of nuclear mass models. The first column is the mass model employed. The last two columns are the weight $\omega$ and the relevant neutron irradiation time $\tau$ (in units of seconds), respectively.

| Mass model | $\omega$ | $\tau$(s) |
|---|---|---|
| RMF | $2.1 \times n_n^{0.020}$ | $0.454 \times n_n^{0.040}$ |
| FRDM | $3.0 \times 10^4 \times n_n^{-0.161}$ | $0.013 \times n_n^{0.075}$ |
| ETFSI-Q | $54.4 \times n_n^{-0.040}$ | $0.499 \times n_n^{0.025}$ |
| HFB13 | $2.8 \times 10^4 \times n_n^{-0.160}$ | $0.007 \times n_n^{0.085}$ |

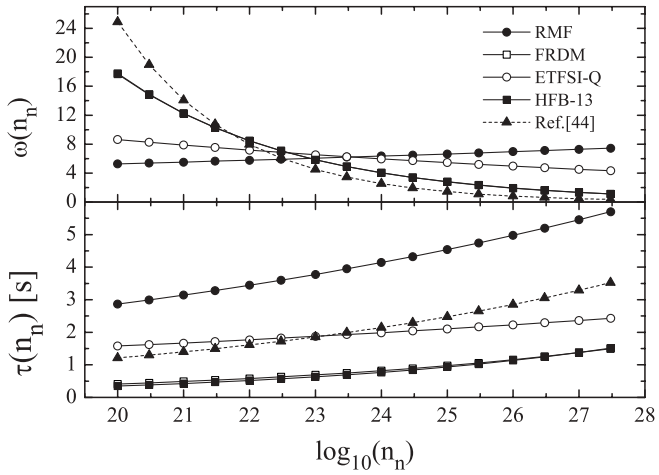


FIG. 7. The best configuration of sixteen $r$-process components that reproduce the solar system $r$-process abundances with different mass inputs at temperature $T = 1.5$ GK. The neutron density $n_n$ is in units of cm$^{-3}$. The weighting factor $\omega(n_n)$ and the neutron irradiation time $\tau(n_n)$ are shown in the upper and lower panels as a function of neutron density $n_n$. In the upper panel, the weighting factors for the FRDM are completely overlaid by those for the HFB-13 models. The fit from Ref. [47] is also plotted for comparison. The total weighting factor has been normalized to 100.

durations are somewhat in between. Moreover, it may be worth mentioning that the simulations using the FRDM and HFB-13 masses demand almost identical astrophysical conditions. A similar calculation based on the ETFSI-Q mass model was carried out in Ref. [47] with a lower temperature $T = 1.35$ GK. As shown in Fig. 7, their obtained neutron irradiation times are in good agreement with our calculation using the ETFSI-Q masses and FRDM half-live inputs, but the weighting factors differ. The superposition obtained in Ref. [47] demands a sharper evolution of the weighting factor as a function of $n_n$. Since a lower temperature of $T = 1.35$ GK in our calculations only weakly impacts the condition obtained, the difference should be due to the different $\beta$-decay properties used in that work. Based on a full dynamical network calculation, faster time scales, of the order of hundreds of milliseconds, are found in Ref. [53] for an $r$-process in the neutron-wind scenario of core-collapse type II supernovae. However, this different time scale can be at least partially attributed to different seed nuclides. In their calculation, the $r$-process starts from a seed distribution containing neutron-rich nuclei with mass numbers between 80 and 100, whereas ours starts from $^{56}$Fe.

Solar $r$-process abundances after $\beta$ decays calculated by using different mass models are displayed in Fig. 8. Shadowed areas show the regions with underproduced abundances before the neutrons freeze out. After $\beta$ decays to the stability line, these gaps are too large to be completely filled in by $\beta$-delayed neutron emissions. It should be pointed out that the solar system $r$-process abundances are defined as the abundances not produced in the $s$-process and $p$-process that still have to be created elsewhere to explain the actual solar system abundances. Although it is thought that the $r$-process is responsible for the majority of those isotopic abundances with $Z \geqslant 56$, its contribution to the lighter elements is still debatable [54,55]. It is possible that some of the discrepancies in the reproduction of the low-mass abundances may be due to an additional nucleosynthesis component creating some of those abundances. However, since astrophysical conditions and nuclear properties both affect the resulting $r$-process abundances, one needs to determine or at least understand the uncertainty in the nuclear physics properties in any future work to disentangle the two effects [56]. In this paper we only discuss possible nuclear physics reasons for such underabundances.

The $r$-process abundances calculated with all nuclear mass models result in abundance underproduction at $A \sim 120$ and $A \sim 170$. Traditionally, the underestimation of the isotopic abundances before the $A \sim 130$ peak has been attributed to the overestimated strength of the $N = 82$ shell closure [8,47,51] in the theoretical nuclear physics model even though the experimental evidence is still debated [57–59]. Since it is not possible to do a complete study of the shell-quenching effect at the single-particle level, which should affect more nuclei than the one with $N = 82$, we only study the effect of a reduced shell closure by artificially decreasing the shell gap energies at $N = 82$ in the RMF and FRDM models by 2 and 1 MeV, respectively. In such a way, the shell gaps of interest for the $r$-process would roughly have the same values as those in the quenched models ETFSI-Q and HFB-13. Eventually, a better agreement with the observation at $A \sim 120$ is obtained, as shown in Figs. 8(a) and 8(b). This can be easily understood as follows. A reduction of shell gap leads to a nuclear matter repopulation in the isotopic chain according to Eq. (3). The $r$-process waiting points located at $N = 82$ move closer to the valley of stability and thus some of the underabundance can be filled. Furthermore, based on Fig. 3 one could expect that the quenched shell gap at $N = 82$ would not affect the abundance around $A \sim 115$. It is interesting to note that the $r$-process simulation using the shell-quenched ETFSI-Q model in Fig. 8(c) show good agreement with the solar abundance pattern at $A \sim 120$ together with a large underproduction at a lower mass number $A \sim 115$.

The abundance trough at $A \sim 115$ for the FRDM, RMF, and ETFSI-Q models can be related to the additional bump of $S_n$ at $A = 110$–$120$ in Fig. 3 and thus to the associated nuclear shape transition. In the case of the ETFSI-Q model, nuclear shape changes from prolate to oblate and then to spherical nuclei with $N = 82$. This transition leads to a deviation from the approximate relationship between neutron separation energies and mass number for each isotope, as can be clearly recognized in Fig. 3(c) by the sudden increase of the separation energies. To highlight the sensitivity of the $r$-process calculation to the effect of the nuclear shape transition, we lowered the separation energies of $^{118,120}$Mo by 1 MeV in the ETFSI-Q model, but we kept the other nuclear physics input unchanged. Those isotopes are in the $r$-process path and show a bump in the one-neutron separation energies as a function of mass number. As shown in Fig. 8(c) the $A \sim 115$ trough is largely filled in. A similar analysis leads to the same conclusion for the FRDM and RMF mass models. Although we have mainly focused on the underabundance below $N = 82$, a similar conclusion can be drawn for the trough around $A \sim 170$. As an example, Fig. 8(b) shows that the trough is almost completely filled in by lowering the separation energies of $^{185}$Pm and $^{186}$Sm by

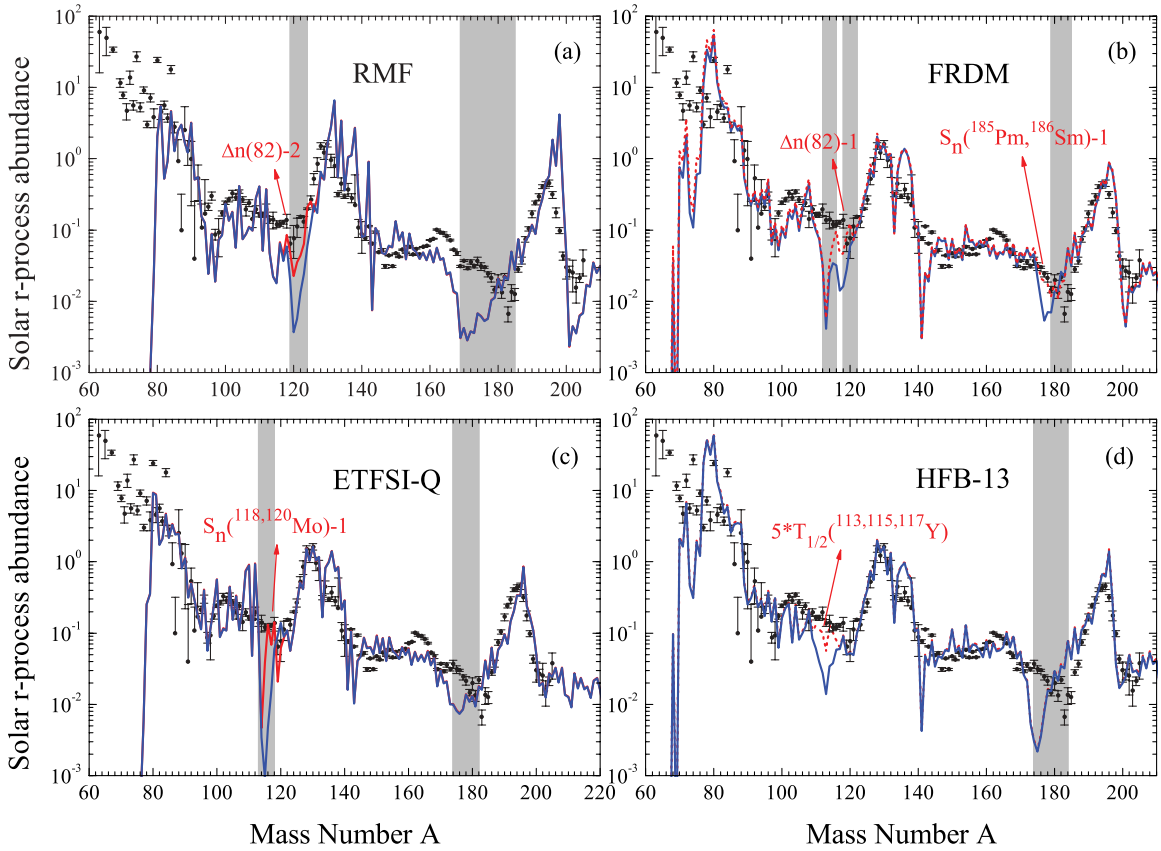


FIG. 8. (Color online) Our best fits to the solar $r$-process abundances (in the logarithm scale) using different nuclear mass inputs. The $\beta$-decay properties are taken from the FRDM model [49]. The best fits are displayed as blue-solid lines. In the sub-figure (a), the red-dashed curve is the same as the blue-solid curve but with a shell closure at $N = 82$ 2 MeV smaller. In the sub-figure (b), the red-dashed curve is the same as the blue-solid curve but with a shell closure at $N = 82$ 1 MeV smaller and separation energies of $^{185}$Pm and $^{186}$Sm 1 MeV smaller. In the sub-figure (c), the red-dashed curve is the same as the blue-solid curve but with separation energies of $^{118,120}$Mo 1 MeV smaller. In the sub-figure (d), the red-dashed curve is the same as the blue-solid curve but with half-live of isotopes $^{113,115,117}$Y five times larger . The shadowed areas correspond to the range where the abundances of these isotopes are largely underestimated before neutrons freeze-out.

1 MeV. This suggests that the potentially wrongly assigned location of the shape transition before the neutron magic number in the theoretical predictions can lead to troughs before the abundance peaks.

Of all the mass models, the HFB-13 model is the only one that shows a smooth one-neutron separation energy change from Sr to Ru. As a result, the $r$-process waiting points are continuous and there is no apparent gap in the $r$-process path [see Fig. 3(d)]. Only modifications in the nuclear masses would not result in the filling of the abundance gap at $A \sim 115$. Such underproduction may be traced back to the $\beta$-decay properties. By increasing the $\beta$-decay half-lives of the critical nuclei $^{113,115,117}$Y by a factor of 5, we found that the trough before the $A \sim 130$ peak in the HFB-13 case can be nearly filled in, as shown in Fig. 8(d).

## V. SUMMARY

We have applied the most recent comprehensive mass models, the nonrelativistic microscopically rooted HFB-13 and the relativistic RMF, to $r$-process calculations. For the sake of comparison, we also included the widely used macro-microscopic models FRDM and ETFSI-Q. Of these models, the HFB-13 and RMF models are used for the first time in such calculations. Based on a simple $r$-process model, it is found that all mass models reproduce the main features of the solar $r$-process pattern and the position of the abundance peaks. Since $r$-process simulations have to rely on predicted nuclear physics properties of unknown regions in the nuclear chart, we have compared the predictions of different mass models. We have also made a systematic study of the influence of the mass model uncertainty in the application of the $r$-process and thus in the required astrophysical conditions. This nuclear physical uncertainty is very important for a complete understanding of the $r$-process since the results of more modern fullly dynamic $r$-process calculations depend on the nuclear mass input used. It is found that the deduced astrophysical conditions such as the neutron irradiation time of the $r$-process can be significantly different depending on the mass model used. Among the different models, the simulation using the RMF masses requires a longer time scale (up to a factor of 4)

than those using FRDM and HFB-13 models. Furthermore, it is found that the optimal astrophysical conditions obtained by using the ETFSI-Q and RMF mass models require a relatively constant weighting factor for neutron densities in the range $10^{22}$ to $10^{28}$ cm$^{-3}$, whereas the FRDM and HFB-13 simulations favor a large weighting factor at low densities. In addition, we have explored the possible deficiencies in different mass models and found that the observed abundance underproduction before the abundance peaks in all the models can be a combined and complex effect of both shell structure and shape transition. An exception is the underproduction at $A \sim 115$ in the HFB-13 model, which can be attributed to incorrect $\beta$-decay rates. Future experiments are needed to determine the strength of the shell closure toward the neutron dripline as well as the precise locations of the shape transition toward the shell-closures.

## ACKNOWLEDGMENTS

We thank C. Scheidenberger for his interest of this work, G. Martinez Pinedo and B. Pfeiffer for valuable discussions, J. M. Pearson for providing the ETFSI-Q and HFB-13 mass tables, and P. Möller for the $\beta$-decay data. This work is partly supported by Major State Basic Research Developing Program No. 2007CB815000 and the National Natural Science Foundation of China under Grant Nos. 10435010, 10775004, and 10221003.

[1] I. Tanihata *et al*., Phys. Rev. Lett. **55**, 2676 (1985).
[2] W. Schwab *et al*., Z. Phys. A **350**, 283 (1995).
[3] J. J. Cowan, F.-K. Thieleman, and J. W. Truran, Phys. Rep. **208**, 267 (1991).
[4] Y.-Z. Qian, Prog. Part. Nucl. Phys. **50**, 153 (2003).
[5] E. M. Burbidge, G. R. Burbidge, W. A. Fowler, and F. Hoyle, Rev. Mod. Phys. **29**, 4 (1957).
[6] E. R. Hilf, H. V. Groote, and K. Takahashi, in *Proceedings of the Third International Conference on Nuclei Far from Stability* (CERN, Geneva, 1976), p. 142.
[7] K.-L. Kratz, J.-P. Bitouzet, F.-K. Thielemann, P. Möller, and B. Pfeiffer, Astrophys. J. **403**, 216 (1993).
[8] B. Pfeiffer, K.-L. Kratz, and F.-K. Thielemann, Z. Phys. A **357**, 235 (1997).
[9] S. Wanajo, S. Goriely, M. Samyn, and N. Itoh, Astrophys. J. **606**, 1057 (2004).
[10] P. Möller, J. R. Nix, W. D. Myers, and W. J. Swiatecki, At. Data Nucl. Data Tables **59**, 185 (1995).
[11] J. M. Pearson, R. C. Nayak, and S. Goriely, Phys. Lett. **B387**, 455 (1996).
[12] S. Goriely, M. Samyn, P.-H. Heenen, J. M. Pearson, and F. Tondeur, Phys. Rev. C **66**, 024326 (2002).
[13] M. Samyn, S. Goriely, M. Bender, and J. M. Pearson, Phys. Rev. C **70**, 044309 (2004).
[14] S. Goriely, M. Samyn, M. Bender, and J. M. Pearson, Phys. Rev. C **68**, 054325 (2003).
[15] S. Goriely, M. Samyn, and J. M. Pearson, Nucl. Phys. **A773**, 279 (2006).
[16] J. D. Walecka, Ann. Phys. (NY) **83**, 491 (1974).
[17] M. Bender, P.-H. Heenen, and P. G. Reinhard, Rev. Mod. Phys. **75**, 121 (2003).
[18] J. Meng, H. Toki, S. G. Zhou, S. Q. Zhang, W. H. Long, and L. S. Geng, Prog. Part. Nucl. Phys. **57**, 470 (2006).
[19] M. M. Sharma, G. A. Lalazissis, and P. Ring, Phys. Lett. **B317**, 9 (1993).
[20] A. Arima, M. Harvery, and K. Shimizu, Phys. Lett. **B30**, 517 (1969).
[21] K. T. Hecht and A. Adler, Nucl. Phys. **A137**, 129 (1969).
[22] J. N. Ginocchio, Phys. Rev. Lett. **78**, 436 (1997).
[23] J. Meng, K. Sugawara-Tanabe, S. Yamaji, P. Ring, and A. Arima, Phys. Rev. C **58**, R628 (1998).
[24] J. Meng, K. Sugawara-Tanabe, S. Yamaji, and A. Arima, Phys. Rev. C **59**, 154 (1999).
[25] T. S. Chen, H. F. Lu, J. Meng, S. Q. Zhang, and S. G. Zhou, Chin. Phys. Lett. **20**, 358 (2003).
[26] S. G. Zhou, J. Meng, and P. Ring, Phys. Rev. Lett. **91**, 262501 (2003).
[27] D. Hirata, K. Sumiyoshi, I. Tanihata, Y. Sugahara, T. Tachiba, and H. Toki, Nucl. Phys. **A616**, 438 (1997).
[28] G. A. Lalazissis, S. Raman, and P. Ring, At. Data Nucl. Data Tables **71**, 1 (1999).
[29] N. Sandulescu, N. Van Giai, and R. J. Liotta, Phys. Rev. C **61**, 061301(R) (2000).
[30] L. S. Geng, H. Toki, S. Sugimoto, and J. Meng, Prog. Theor. Phys. **110**, 921 (2003).
[31] L. S. Geng, H. Toki, and J. Meng, Prog. Theor. Phys. **113**, 785 (2005).
[32] H. Geissel *et al*., AIP Conf. Proc. **831**, 108 (2006).
[33] G. Audi, A. H. Wapstra, and C. Thibault, Nucl. Phys. **A729**, 337 (2003).
[34] P. Marmier and E. Sheldon, *Physics of Nuclei and Particles*, Vol. I (Academic Press, New York, 1971).
[35] S. E. Woosley and R. D. Hoffman, Astrophys. J. **395**, 202 (1992).
[36] K. Takahashi, J. Witti, and H.-Th. Janka, Astron. Astrophys. **286**, 857 (1994).
[37] S. Wanajo, T. Kajino, G. J. Mathews, and K. Otsuki, Astrophys. J. **554**, 578 (2001).
[38] T. A. Thompson, A. Burrows, and B. S. Meyer, Astrophys. J. **562**, 887 (2001).
[39] C. Freiburghaus, S. Rosswog, and F.-K. Thielemann, Astrophys. J. **525**, 121 (1999).
[40] S. Rosswog, M. Liebendörfer, F.-K. Thielemann, M. B. Davies, W. Benz, and T. Piran, Astron. Astrophys. **341**, 499 (1999).
[41] S. Goriely, P. Demetriou, H.-Th. Janka, J. M. Pearson, and M. Samyn, Nucl. Phys. **A758**, 587 (2005).
[42] A. G. W. Cameron, Astrophys. J. **562**, 456 (2001).
[43] H. Ning, Y.-Z. Qian, and B. S. Meyer, Astrophys. J. Lett. **667**, L159 (2007).
[44] R. Surman and G. C. McLaughlin, Nucl. Phys. **A758**, 189 (2005).
[45] J. J. Cowan, J. E. Lawler, C. Sneden, E. A. D. Hartog, and J. Collier, in *Proceedings of the NASA Laboratory Astrophysics Workshop*, edited by P. F. Weck, H. S. Kwong, and F. Salama (2006), p. 82; astro-ph/0605137.
[46] K.-L. Kratz, K. Farouqi, B. Pfeiffer, J. W. Truran, C. Sneden, and J. J. Cowan, Astrophys. J. **662**, 39 (2007).

[47] J. J. Cowan, B. Pfeiffer, K.-L. Kratz, F.-K. Thielemann, C. Sneden, S. Burles, D. Tyler, and T. C. Berrs, Astrophys. J. **521**, 194 (1999).
[48] F. Käppeler, H. Beer, and K. Wisshak, Rep. Prog. Phys. **52**, 945 (1989).
[49] P. Möller, J. R. Nix, and K.-L. Kratz, At. Data Nucl. Data Tables **66**, 131 (1997); P. Möller, B. Pfeiffer, and K.-L. Kratz, Phys. Rev. C **67**, 055802 (2003).
[50] National Nuclear Data Center, http://www.nndc.bnl.gov.
[51] B. Chen, J. Dobaczewski, K.-L. Kratz, K. Langanke, B. Pfeiffer, F.-K. Thielemann, and P. Vogel, Phys. Lett. **B355**, 37 (1995).
[52] H. Schatz, R. Toenjes, B. Pfeiffer, T. C. Beers, J. J. Cowan, V. Hill, and K.-L. Kratz, Astrophys. J. **579**, 626 (2002).
[53] K. Farouqi *et al*., Nucl. Phys. **A758**, 631c (2005).
[54] C. Travaglio, R. Gallino, E. Arnone, J. Cowan, F. Jordan, and C. Sneden, Astrophys. J. **601**, 864 (2004).
[55] F. Montes *et al*., Astrophys. J. **671**, 2, 1685 (2007).
[56] B. Sun and J. Meng, Chin. Phys. Lett. **25**, 2429 (2008).
[57] I. Dillmann *et al*., Phys. Rev. Lett. **91**, 162503 (2003).
[58] W. B. Walters *et al*., Phys. Rev. C **70**, 034314 (2004).
[59] A. Jungclaus *et al*., Phys. Rev. Lett. **99**, 132501 (2007).